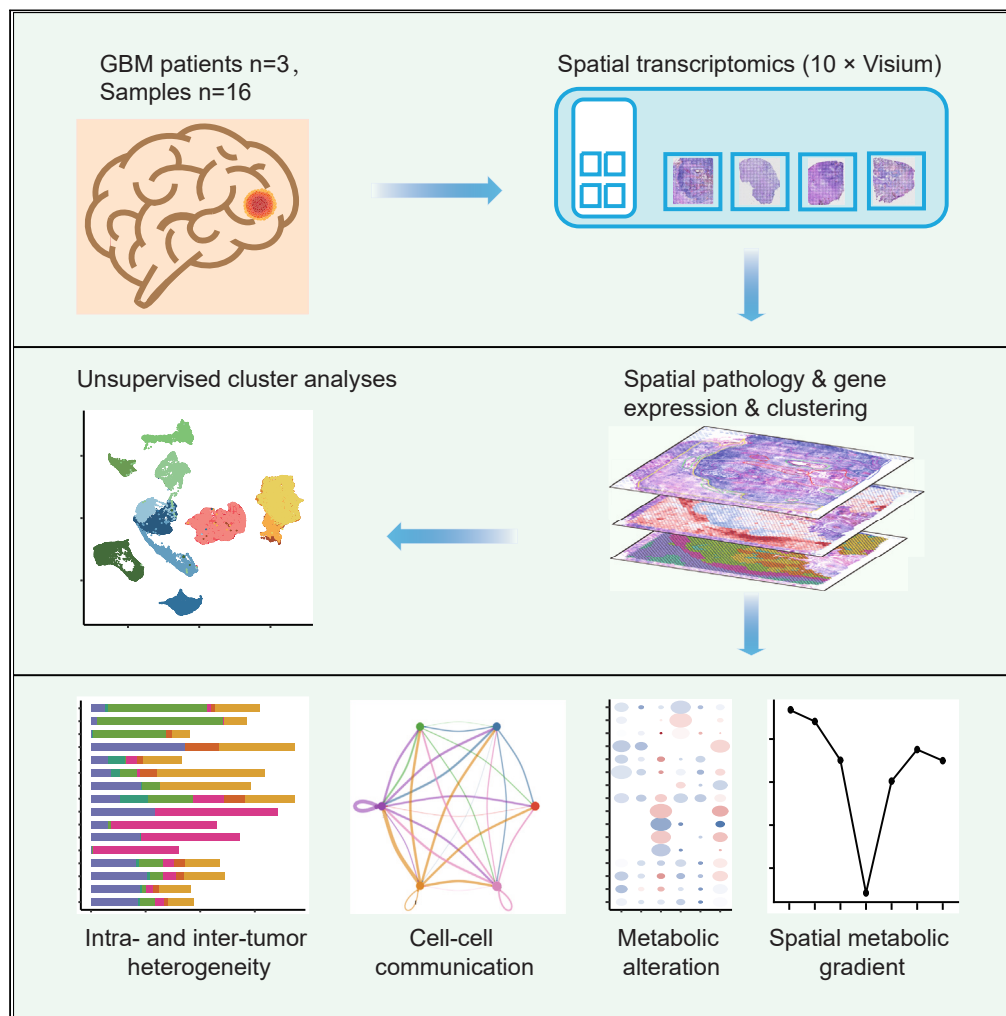**Article**

Decoding heterogeneous and coordinated tissue architecture in glioblastoma using spatial transcriptomics

Xuejiao Lv, Bo Wang, Kunlun Liu, Mulin Jun Li, Xianfu Yi, Xudong Wu

yixianfu@tmu.edu.cn (X.Y.)
wuxudong@tmu.edu.cn (X.W.)

Highlights

Spatial transcriptomic studies have revealed extensive intra-GBM heterogeneity

Tissue stem cell signatures are correlated with mesenchymal subtype

Key signaling networks for the intercellular communication are identified

Different pathological zones exhibit common or varied metabolic states

Article

Decoding heterogeneous and coordinated tissue architecture in glioblastoma using spatial transcriptomics

Xuejiao Lv,[1,2,6] Bo Wang,[3,6] Kunlun Liu,[4] Mulin Jun Li,[4] Xianfu Yi,[4,*] and Xudong Wu[1,5,7,*]

SUMMARY

Glioblastoma multiforme (GBM) is one of the most lethal brain tumors, characterized by profound heterogeneity. While single-cell transcriptomic studies have revealed extensive intra-tumor heterogeneity, shed light on intra-tumor diversity, spatial intricacies remain largely unexplored. Leveraging clinical GBM specimens, this study employs spatial transcriptomics technology to delve into gene expression heterogeneity. Our investigation unveils a significant enrichment of tissue stem cell signature in regions bordering necrosis and the peritumoral area, positively correlated with the mesenchymal subtype signature. Moreover, upregulated genes in these regions are linked with extracellular matrix (ECM)-receptor interaction, proteoglycans, as well as vascular endothelial growth factor (VEGF) and angiopoietin-Tie (ANGPT) signaling pathways. In contrast, signatures related to glycogen metabolism and oxidative phosphorylation show no relevance to pathological zoning, whereas creatine metabolism signature is notably exclusive to vascular-enriched areas. These spatial profiles not only offer valuable references but also pave the way for future in-depth functional and mechanistic investigations into GBM progression.

INTRODUCTION

Glioblastoma multiforme (GBM) is an archetypal example of a heterogeneous cancer and one of the most lethal human malignancies.[1,2] Patients diagnosed with GBM have a median survival between 12.2 and 18.2 months, even with standard treatment of maximum surgical resection followed by radiotherapy, chemotherapy, and/or immunotherapy.[3] This underscores the critical need for extensive research on GBM to establish a solid theoretical foundation for advancing clinical treatment strategies.

The advent of massively parallel DNA and RNA sequencing has empowered the acquisition of genomic, transcriptomic, and epigenomic information for cells and tissues. Groundbreaking initiatives such as The Cancer Genome Atlas (TCGA) and other comprehensive studies have led to a reevaluation of the World Health Organization's classification of brain tumors, incorporating molecular features. Integrated analyses of multi-omics data from these endeavors have delineated three subtypes of GBMs: proneural (PN), classical (CL), and mesenchymal (MES).[4] Importantly, the MES subtype is associated with a worse prognosis compared to the other two subtypes, attributed to its heightened invasiveness, ability to evade immunosurveillance, and resistance to therapy.[1,5,6] This molecular subtyping has gained increasing recognition as a pivotal prognostic determinant. Notably, these distinct subtypes of tumor cells may coexist within an individual tumor, a phenomenon referred to as intra-tumoral heterogeneity.[4,5]

Traditional methods for characterizing intra-tumoral heterogeneity in tumor tissue rely heavily on established histological and molecular markers, often requiring microscopic evaluations by skilled pathologists. However, over the past decade, the emergence of single-cell RNA-sequencing (scRNA-seq) techniques have revolutionized the analysis of gene expression heterogeneities in individual cells, offering insights into cell fate decisions.[4,7–9] scRNA-seq datasets have provided intricate details about patterns of cell-cell communications and identified key regulators of stemness and cell plasticity.[10–12] However, the process of sorting single cells from a suspension of dissociated tissues inevitably results in the loss of spatial information. To address this limitation, Yu et al. conducted single-cell analysis on multi-sector biopsies guided by precision navigation surgery. This innovative approach provided the first spatial-level analysis of cellular states within human gliomas, offering

[1]State Key Laboratory of Experimental Hematology, The Province and Ministry Co-sponsored Collaborative Innovation Center for Medical Epigenetics, Tianjin Key Laboratory of Medical Epigenetics, Key Laboratory of Immune Microenvironment and Disease (Ministry of Education), Department of Cell Biology, School of Basic Medical Sciences, Tianjin Medical University, Tianjin 300070, China
[2]Department of Occupational and Environmental Health, School of Public Health, Tianjin Medical University, Tianjin 300070, China
[3]Department of Neurosurgery, Clinical College of Neurology, Neurosurgery and Neurorehabilitation, Tianjin Medical University, Tianjin Huanhu Hospital, Tianjin Key Laboratory of Cerebral Vascular and Neurodegenerative Diseases, Tianjin Neurosurgical Institute, No. 6 Jizhao Road, Tianjin 300350, China
[4]Department of Bioinformatics, School of Basic Medical Sciences, Tianjin Medical University, Tianjin 300070, China
[5]Tianjin Key Laboratory of Spine and Spinal Cord, Tianjin Medical University General Hospital, Tianjin, China
[6]These authors contributed equally
[7]Lead contact
*Correspondence: yixianfu@tmu.edu.cn (X.Y.), wuxudong@tmu.edu.cn (X.W.)
https://doi.org/10.1016/j.isci.2024.110064

a molecular map of the interactions between tumor cells and the surrounding stroma cells at a single-cell resolution.[10] Despite these advancements, the dissociation of tissue before sequencing remains a challenge, leading to the unavoidable loss of detailed architectural information.

In response to this challenge, the recently developed spatial transcriptomics (ST) method integrates the advantages of traditional spatially resolved technologies, such as immunohistochemistry (IHC) or *in situ* hybridization, with the high-throughput RNA-seq analysis. This integration enables the unbiased mapping of transcripts across entire tissue sections, offering a comprehensive spatial perspective.[13,14] ST technology has found applications across a diverse range of studies, spanning organ development and investigations into various diseases.[15–18] Within the realm of diseases, this technology has been extensively employed to probe into tumor heterogeneity and immune infiltration.[17–19] Notably, recent studies have established a spatial correlation between T cell exhaustion and mesenchymal-like gene expression in GBM.[18] In addition, other high-sensitivity ST techniques such as Slide-seq, Slide-seqV2, DBiT-seq, and the 10X Genomics Xenium platform have also been widely used in the directed spatial analysis of transcription and protein expression.[20–23] The spatial information regarding the distribution and interactions of tumor cells, stromal cells, and immune cells provides an enriched guiding principle for a deeper understanding of tumor heterogeneity.

Here, we present a spatiotemporal atlas designed to quantify mRNA populations within the spatial context of intact tissue. This atlas systematically characterizes spatial archetypes and cellular heterogeneity across 16 GBM tissue samples obtained from three GBM patients. Through the integration of pathological partitioning, we unravel the correlation between cell types and GBM subtypes, shedding light on the prevalent cell-cell communications within distinct clusters. Additionally, we conduct a comprehensive analysis and comparison of metabolic patterns across various pathological zones. These datasets are poised to provide valuable spatial insights into the expression patterns of genes of interest within the field, thereby contributing to a deeper understanding of the complex spatial and temporal dynamics underlying GBM.

RESULTS

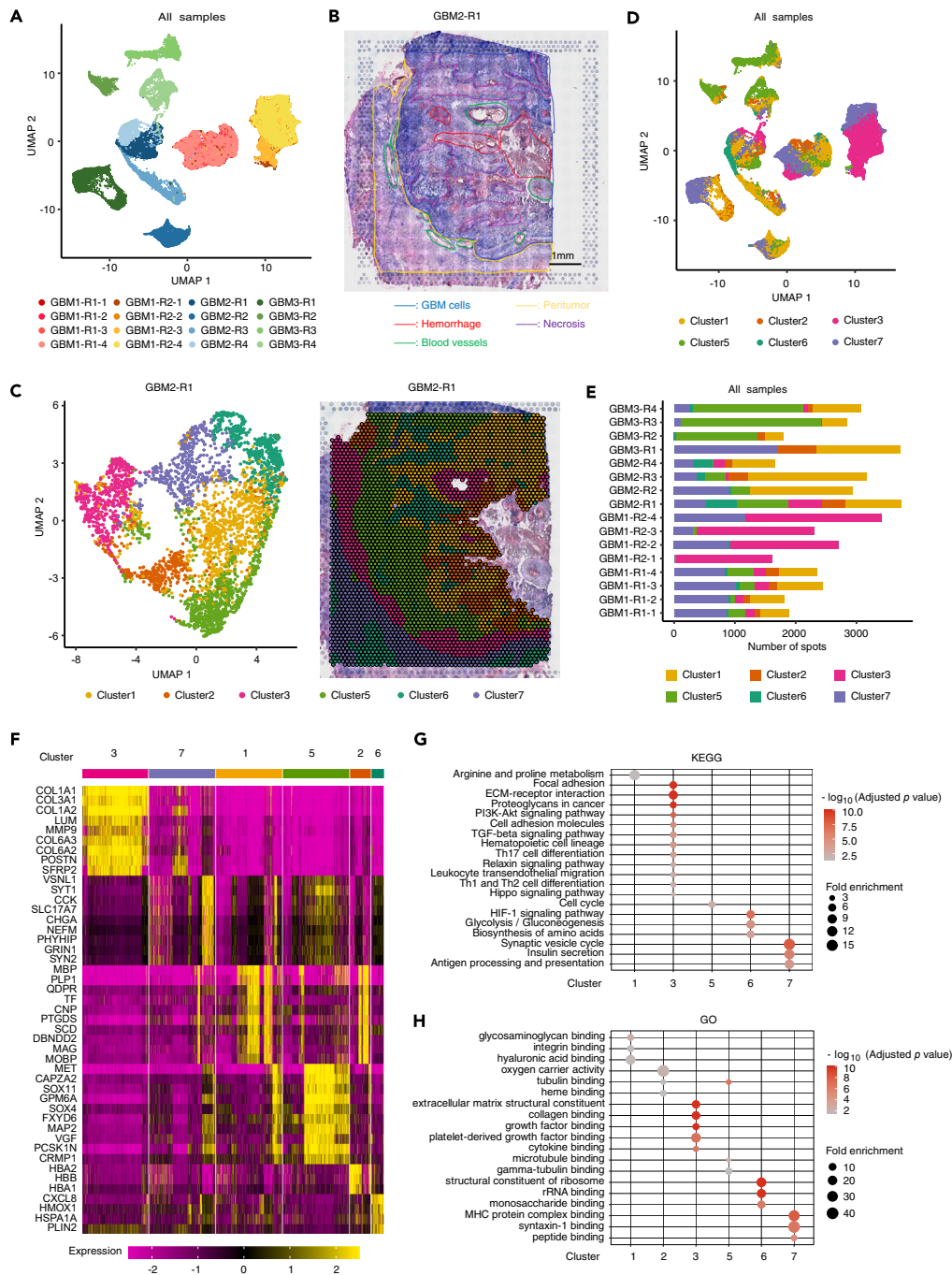### Exploration of GBM architecture with spatial transcriptomics

To comprehensively analyze the spatial heterogeneity, we collected 16 surgical specimens from three patients with newly diagnosed GBM and applied ST analysis via 10× Genomics Visium platform (Figure S1A). All the three patients did not receive radio- or chemotherapy before tumor resection. In this study, a spot contains approximately 2–40 cells (Figure S1B). The median sequencing depth of a single spot is approximately 30,000 unique molecular identifiers (UMIs) and 3,000 genes (Figure S1B; Table S1).

Each individual sample was processed using the R Seurat[24] package and normalized by the sctransform method. Subsequent analysis employing *t*-distributed Stochastic Neighbor Embedding (t-SNE) and Uniform Manifold Approximation and Projection (UMAP) revealed significant distinctions among spot obtained from distinct patients (GBM1 vs. GBM2 vs. GBM3). These spots were distinctly mapped to discrete locations based on their gene expression profiles, as illustrated in Figure S1C. This divergence underscores the pronounced inter-tumor heterogeneity within the dataset. Furthermore, scrutiny of spot obtained from serial sections (GBM1-R1-1 to GBM1-R1-4 and GBM1-R2-1 to GBM1-R2-4) corresponding to specific regions (GBM1-R1 and GBM1-R2, respectively) demonstrated a consistent mapping to the same t-SNE or UMAP coordinates based on gene expression. In contrast, scrutiny of spot from non-serial sections originating from distinct sampling sites (R1 to R4) within the same patients (GBM2 or GBM3) exhibited discrete t-SNE or UMAP coordinates (Figures S1D and 1B). This observation underscores the intra-tumor heterogeneity. The presence of both inter-tumor and intra-tumor heterogeneity collectively attests to the heightened diversity inherent in GBM cellular composition.

We conducted a meticulous histopathological analysis on H&E staining images obtained from 16 sequenced samples, delineating pathological division into five distinct areas: tumor, necrosis, peritumor, hemorrhage, and blood vessel regions (Figure S1F). Notably, GBM2-R1 showcased comprehensive histopathological features, encompassing all five delineated areas with exceptional clarity (Figure 1B). Consequently, GBM2-R1 was selected as an exemplary case for an in-depth analysis.

Applying BayesSpace[25] for integrated clustering analysis on this representative sample, we identified six distinct cellular clusters and subsequently mapped them back to their spatial locations (Figure 1C; Table S2). Remarkably, these clusters exhibited a noteworthy correspondence with the predefined pathological divisions within GBM2-R1. Particularly, striking is the spatial distribution of spots in Cluster 3, predominantly situated in regions enriched with blood vessels, tumor periphery, and tumor junction, whereas Cluster 7 spots were identified in the peritumoral area at the forefront of tumor infiltration into surrounding normal brain tissue (Figures 1B and 1C). Distinctively, Cluster 5 was localized adjacent to blood vessels, displaying the highest cell density, setting it apart from the necrotic areas around the tumor or at the tumor center (Figure 1B). Additionally, other clusters, namely Cluster 1, 2, and 6, were identified within the tumor center, corresponding to areas indicative of tumor necrosis. Ultimately, the established clustering criteria were extrapolated to all 16 samples obtained from three distinct patients (Figures 1D and S2A). The spatial distributions elucidate a comparable consistency between the identified clusters and the predefined pathological divisions across the entire sample set (Figures S2B and S2C). The coherence observed between gene expression profile clustering and pathological divisions not only underscores the presence of intra-tumor heterogeneity but also validates the robustness of the clustering analysis.

In summary, the six identified clusters exhibited distinctive distribution patterns across the sequenced samples. Notably, spots derived from serial sections of GBM1-R1 encompassed representatives from all six feature clusters, whereas serial sections from the same patient, GBM1-R2, predominantly featured spots clustered into Cluster 3 and Cluster 7 (Figure 1E). Although spots assigned to Cluster 5 and Cluster 7 were consistently identified across all sequenced samples, their proportional representation varied significantly among samples. Notably, GBM3-R2~R4 exhibited the highest proportion of spots assigned to Cluster 5 (58.86%–81.21%), whereas GBM1-R2-1~4 displayed the lowest

Figure 1. Exploration of the architecture complexity of GBM through spatial transcriptomics

(A) UMAP (Uniform Manifold Approximation and Projection) plot illustrating the spots from all tissue sections, colored by their respective sample origins.

(B) Histopathological analysis conducted on the hematoxylin and eosin (H&E) stained images of GBM2-R1, providing insights into the histological characteristics. Scale bars, 1 mm.

(C) Application of the BayesSpace method to perform clustering analysis of GBM2-R1, revealing distinct pathological subareas with the tissue. Individual spots are represented as dots, colored based on optimized global clusters.

(D) UMAP plot displaying the spots from all sections, with colors indicating the delineation of optimized global clusters.

(E) Depiction of the distribution pattern of the optimized clusters across the 16 sequenced samples.

(F) Heatmap showing the expression patterns of differentially expressed genes across the identified clusters.

(G) Kyoto Encyclopedia of Genes and Genomes (KEGG) analysis of the differently expressed genes across the identified clusters, offering insights into the associated pathways and biology functions.

(H) Gene Ontology (GO) analysis conducted on the differently expressed genes across various clusters, shedding light on the distinct functional roles of these genes.

values (0%–2.08%; Figure 1E). Cluster 7 similarly demonstrated diverse cellular proportions ranging from 0.06% to 49.12%. Analogously, other clusters displayed similar distribution trends, with Cluster 3 exhibiting the highest ratio in GBM1-R2 (65.86%–98.45%) and Cluster 1 being present in all sequenced samples except GBM1-R2 (Figure 1E). These findings collectively underscore the presence of intra-tumoral and inter-tumoral heterogeneity within GBM at the cellular clustering level.

To further elucidate the pathological significance associated with spot clustered into the six distinct clusters, we performed a differential gene expression analysis, identifying Differentially Expressed Genes (DEGs) for each cluster. The heatmap in Figure 1F highlights the top 10 representative DEGs per cluster, clearly demarcating distinctive gene expression profiles for each cluster. DEGs enrichment analysis, employing the Kyoto Encyclopedia of Genes and Genomes (KEGG) pathways, unveiled intrinsic differences among the clusters. Specifically, Cluster 3 exhibited enrichment in pathways of focal adhesion and extracellular matrix (ECM)-receptor interaction (Figure 1G), indicative of its heightened plasticity within the tumor microenvironment (TME). Concurrently, Gene Ontology (GO) and Reactome analyses corroborated these findings, emphasizing the functions of regulation of extracellular matrix structural constituent, collagen binding, extracellular matrix organization, and degradation of the extracellular matrix (Figures 1H and S3A). In contrast, Cluster 7 demonstrated KEGG enrichment in synaptic vesicle cycle and antigen processing and presentation (Figure 1H), suggesting a composite phenotype reflecting features of both normal brain tissues and infiltrating tumor cells. GO and Reactome analyses further supported these observations, revealing enrichments in major histocompatibility complex (MHC) protein complex binding and transmission across chemical synapses (Figures 1G and S3A). Take GBM2-R1 as a representative case, we conducted a more intricate analysis focusing on Cluster 3 (associated with blood vessels) and Cluster 7 (representative of the peritumoral region) (Figures S3B–S3D). Subsequent enrichment analysis of DEGs provided a more explicit and pronounced delineation of molecular characteristics. Collectively, these data underscore distinct molecular features discernible among the identified clusters.

## Cellular composition analysis and heterogeneity patterns in GBM

To conduct an in-depth analysis of the cellular composition within the sequenced samples, we use the SingleR to perform cell-type annotation based on the Human Primary Cell Atlas (HPCA). When comparing GBM1-R1 and GBM2, a comparable distribution of spots designated as astrocytic was observed (63.27%–68.70% vs. 32.67%–93.04%; Figures 2A and S4A). Remarkably, GBM3 exhibited the highest percentage of spot classified as astrocytes (96.49%–99.96%), whereas GBM1-R2 displayed the utmost proportion of spot assigned to the tissue stem cell type (96.53%–98.01%) (Figures 2A and S4A). Despite the consistent presence of all identified cell types across samples from diverse patients, their relative proportions exhibited considerable variability, even within samples derived from distinct regions of the same patient. This phenomenon underscores the pronounced inter-tumoral and intra-tumoral heterogeneity prevalent in GBM.

A comprehensive examination of cell-type enrichment within distinct clusters was subsequently undertaken for both the merged dataset and individual samples. Notably, certain cell types, such as tissue stem cells, neurons, and astrocytes, demonstrated a pervasive enrichment across all six clusters (Figure 2B). Cluster 3 exhibited a pronounced enrichment specifically with the cell type of tissue stem cells. Remarkably, fibroblasts and mesenchymal stem cells (MSC) manifested exclusive enrichment within Cluster 3 (Figure 2B). Consistent findings were observed in GBM2-R1 and all other samples (Figures 2B and S4B). The heightened presence of tissue stem cells and MSC within Cluster 3 implies an augmented degree of malignancy and enhanced infiltration capacity. Additionally, Cluster 7 displayed a composite composition featuring astrocytes, tissue stem cells, and neurons (Figures 2B and S4B), indicative of the frontier regions of tumor infiltration.

Leveraging gene expression profiles, we computed module scores for each defined cluster by employing markers associated with glioblastoma subtypes (CL, MES, and PN; Table S3). Notably, the gene expression profiles of spots residing in Clusters 3 and 7 exhibited a significant enrichment with the MES subtype across all 16 sequenced samples (0.34–0.60, mean = 0.52 vs. −0.01 to 0.38, mean = 0.23; Figure 2C). In contrast, neither the PN nor the CL subtype demonstrated a significant enrichment in any spot cluster (−0.18 to 0.24, mean = −0.03 and −0.08 to 0.11, mean = 0.003 for PN and CL, respectively; Figure 2C). To elucidate spatial heterogeneity, we assessed the expression patterns of established markers associated with different GBM subtypes. Notably, in GBM2-R1, the expression of MES markers CD44 and vascular endothelial growth factor A (VEGFA) exhibited a pronounced elevation, followed by the PN markers OLIG2 and EZH2, whereas the CL markers FGFR3 and CDH4 were observed at comparatively lower levels (Figure S5A), further confirming the intra-tumoral heterogeneity with regard to spatial distribution.

Furthermore, upon mapping spots with the MES subtype to the H&E staining image, a conspicuous observation emerged, revealing their predominant localization in regions characterized by a heightened density of blood vessels and situated at the interface between the tumor and the peritumoral area of pathological classification in GBM2-R1 (Figures 1B and 2D). Additionally, spots exhibiting the MES subtype demonstrated a positive correlation with the tissue stem cell signature (R = 0.84, $p < 2.2e\text{-}16$; Figure 2E). While there was minimal enrichment of PN subtype spots, CL subtype spots were only marginally enriched in Cluster 5, positioned within the tumor area adjacent to spots of Cluster 3. Notably, spots displaying the PN or CL subtype exhibited no significant correlation with the tissue stem cell signature (R = −0.0024, p = 0.98, and R = −0.17, p = 0.13, respectively; Figures S5B–S5E).

Notably, quiescent cancer stem cells present different transcriptional characteristics from proliferating counterparts. More importantly, quiescent GBM stem cells drive the initiation, expansion, and recurrence of tumors after chemotherapy.[26] Accordingly, we analyzed Cluster 3 based on the concept of quiescent cancer stem cells defined by the research of Xie et al. and found that the quiescent cancer stem cell signature was significantly enriched in both the integrated analysis of 16 samples and the standalone analysis of GBM2-R1 (Figure 2F). These findings collectively demonstrate that the enrichment of tissue stem cell types and MES subtypes in the GBM sample, specifically in Cluster 3, aligns molecularly with the malignant nature of the disease.
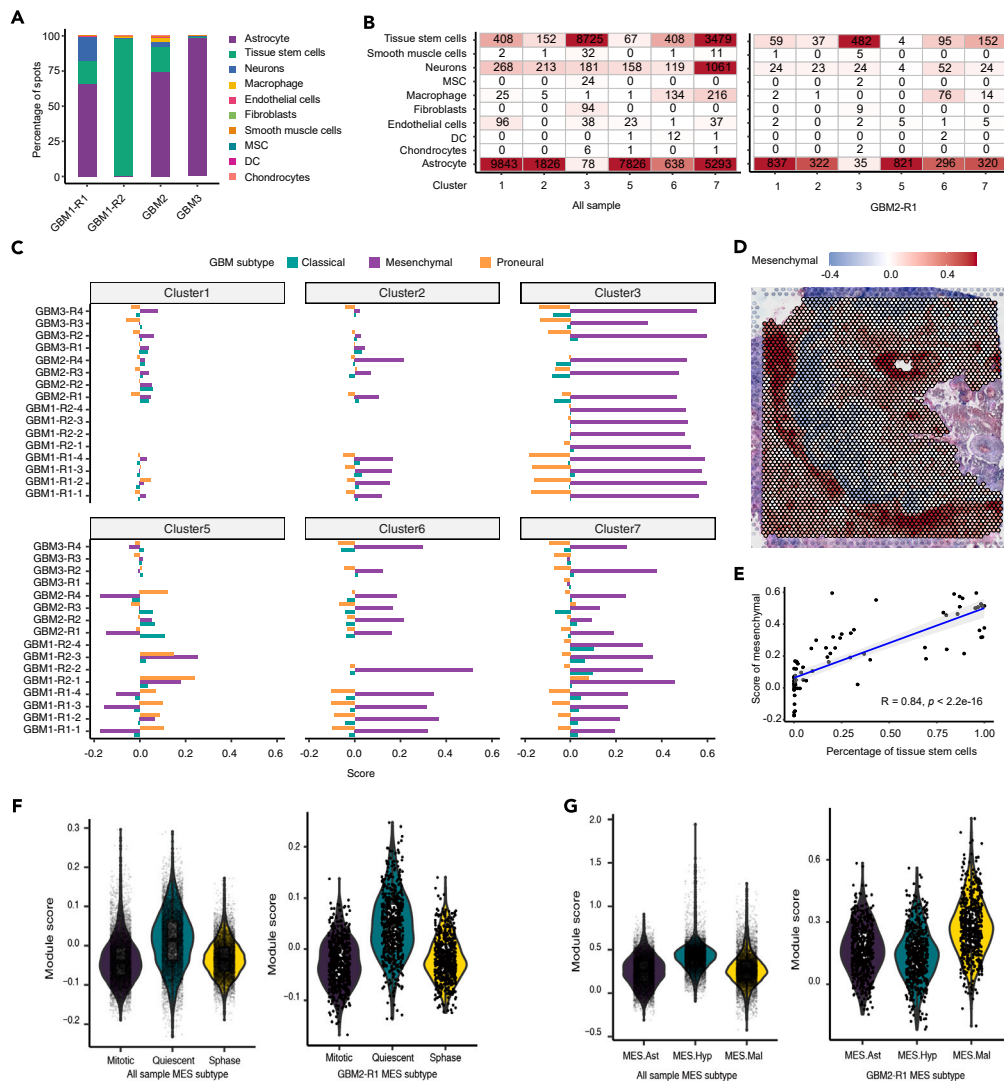
Figure 2. Characterizing inter-tumoral and intra-tumoral heterogeneity in GBM

(A) Distribution of major cell types across patients.

(B) Examination of the enrichment patterns of distinct cell types within various clusters observed in all samples and in the specific case of GBM2-R1.

(C) Relationships based on the correlation analysis between the defined clusters and the GBM molecular subtypes.

(D) Spatial mapping illustrating the distribution of MES subtypes within the GBM2-R1 sample.

(E) Correlation analysis unraveling the associations between the MES subtypes and tissue stem cell types within the context of GBM2-R1. p value was calculated using two-sided Student's t test.

(F) Violin plot analysis of quiescent cancer stem cells in Cluster 3.

(G) Violin plot analysis of three signatures (MES-Hyp, MES-Ast, MES-mal) in Cluster 3.

According to recent studies, diverse MES states exist in glioblastoma with distinct functional, genetic, and environmental associations, leading to variations in clinical prognosis.[27,28] To determine how these MES states are prevalent in our work, we initially analyzed our data using 10 GBM MES signatures summarized by Chanoch-Myers. We found that Cluster 3 is highly enriched for MES_CORE and MHCI isoforms, both in the integrated analysis of 16 samples and in the separate analysis of GBM2-R1. Notably, MHCII is also significantly enriched in the integrated analysis of the 16 samples (Figures S6A and S6B). Subsequently, we analyzed the data with three GBM signatures defined by Greenwald and observed enrichment of all three signatures (MES-Hyp, MES-Ast, and MES-mal) (Figure 2G). Nevertheless, MES-Hyp is significantly enriched in the integrated analysis of 16 samples, whereas MES-mal is significantly enriched in GBM2-R1. Therefore, the marked differential enrichment of MES subtypes within Cluster 3 signifies a profound level of intra- and inter-tumoral heterogeneity in GBM. These data prompt us to conduct a more comprehensive investigation into how distinct MES subtypes influence the pathogenesis and prognosis of GBM in the future.

CellChat reveals spatial crosstalk signaling network in GBM

Intercellular communication is paramount for the proper functioning of multicellular organisms, with cells exchanging information through the secretion of soluble factors or direct interactions.[29] Tumor cells reside in a complex TME composed of diverse stromal cells, including immune cells and fibroblasts, as well as the extracellular matrix.[30] Communication between tumor and non-tumor cells, facilitated by ligand/receptor cross-talks within the glioma TME, has been shown to promote tumor aggressiveness.[10] Additionally, communication among non-tumor cells is characterized by the predominant influence of the CXCL family of chemokines and their associated receptors, particularly noticeable in M2b macrophages and neutrophils.[10] The TME and intercellular communication among TME components are increasingly acknowledged as a pivotal facilitator in the progression of GBM, exerting a critical influence on tumor development.[10,31–33]

To delineate spatially specific ligand-receptor interactions between clusters, we conducted crosstalk signaling network analysis using CellChat,[34] a tool capable of quantitatively infer and analyze intercellular communication networks from single-cell RNA sequencing (scRNA-seq) data.[34] Among the 58 distinct ligand-receptor pairs identified across different clusters in the 16 samples, the ligand-receptor interaction networks involving VEGF, ANGPT, PERIOSTIN, TGFβ, and PDGF were significantly enriched in GBM patients (Figure 3A; Table S4). Notably, the senders and receivers were distinct for each ligand-receptor interaction. The signaling of VEGF was predominantly received by Cluster 3 while being emitted by all clusters (Figures 3A and S7A). In contrast, the signals of ANGPT, PERIOSTIN, TGFβ, and PDGF were primarily sent by Cluster 3 and received by all clusters (Figures 3A and S7B). The intricate sender-receiver pairs underscore the frequent intercellular communication within the TME and emphasize the necessity of spatial information in the study of GBM.

The VEGF signaling pathway, along with its downstream ANGPT signaling pathway, has been implicated not only in angiogenesis and vascular permeability but also in the initiation, progression, and recurrence of tumors, as well as in the generation and preservation of cancer stem cells (CSCs).[35,36] In accordance with previous research, Cluster 3 spots, displaying a significant degree of malignancy, exhibit an enrichment of VEGF signaling. Given the notable enrichment of both VEGF and ANGPT signaling in our samples, crucial in tumor progression, we conducted an in-depth analysis of the VEGF signaling pathway in the GBM2-R1 sample (Figure 3B). Unsurprisingly, our analysis aligns with the comprehensive results from all samples. The findings suggest that in GBM2-R1, spots within Cluster 3, situated in the vascular-enriched area, predominantly receive VEGF signaling. Moreover, all six clusters could potentially function as signal transmitters (Figure 3B). Regarding ANGPT signaling, Cluster 3 spots emerge as the primary source of ANGPT ligands, in addition to serving as the primary recipients of this signaling (Figures 3B and S7B). The reception of VEGF and transmission of ANGPT by Cluster 3 not only align with the upstream-downstream dynamics of these two signaling pathways but also imply the aggressive nature and potential promotion of tumor development within Cluster 3.

Notably, both ANGPT- and VEGF-targeting drugs have demonstrated efficacy in inhibiting tumor growth and reducing tumor burden. The synergistic application of agents targeting both pathways has yielded significantly enhanced anti-tumor and anti-angiogenic effects.[37,38] In a granular examination, ligand-receptor analysis pinpointed VEGFA and VEGFB as the primary transmitters of the upstream VEGF signaling pathway in our samples, with VEGFR1 and VEGFR2 emerging as the principal receptors (Figure 3C). Given the prominent expression of the VEGFS ligand-receptor pair in the spots within our samples, we substantiated the involvement of receptor-ligand interactions in tumor progression using the GBM cell line U87. Utilizing short hairpin RNA (shRNA) constructs targeting VEGF receptor 1 and 2 (VEGFR1/2) to disrupt the ligand-receptor interaction, the Transwell assay revealed a substantial attenuation in the migration capability of U87 cells (Figure 3D). Furthermore, the knockdown of VEGFR1/2 significantly abrogated the sphere formation capacity of U87 cells (Figure 3E). In light of the preceding signaling pathway enrichment analysis and the corresponding experimental validations, it becomes evident that the pronounced enrichment of upstream VEGF and downstream ANGPT signaling pathways play a pivotal role in sustaining the high malignancy traits of GBM.

Deciphering metabolic landscapes in GBM

Metabolic reprogramming emerges as a distinctive hallmark of cancer, endowing cells to generate ample energy and biosynthetic precursors, thereby propelling malignant cellular proliferation.[39,40] A previous study highlighted the intricate link between metabolic reprogramming steering gliomagenesis and aberrations in amino acid, lipid, and peptide metabolism.[40] To elucidate metabolic alterations in GBM patients, we conducted metabolomic profiling, referencing the altered metabolic pathways identified in Prabhu AH's publication (Table S5).[40] Our analysis of ST RNA-seq data revealed prominent enrichment of glycogen metabolism and oxidative phosphorylation (OXPHOS) in all six distinct clusters among the 16 sequenced samples from three patients, regardless of their pathological location (Figure 4A). This suggests that the heightened Glycogen metabolism in tumors is harnessed to sustain cancer cell growth. Notably, the observed OXPHOS enrichment aligns with previous findings indicating the frequent upregulation of this metabolic pathway in cancer tissues. Despite the simultaneous enhancement of glycolysis, OXPHOS serves to provide ATP, thereby promoting tumor proliferation, survival, and genomic stability.[41] Similarly, glycolysis and gluconeogenesis were prominently enriched in all spots, irrespective of their pathological location (Figure 4A). This discovery corresponds with earlier research indicating that the upregulation of glycolysis and gluconeogenesis pathways facilitates the rapid synthesis of metabolic intermediates essential for macromolecular biosynthesis.[42] Furthermore, it enhances the reduction of harmful reactive oxygen species (ROS), thereby sustaining cell proliferation and viability.[41,42] Consequently, our findings underscore a pronounced cancer-specific metabolic profile in malignant GBM.

Creatine, a naturally occurring nitrogen-containing organic acid present in mammals, facilitates sustained energy for cell growth through the interconversion between creatine and phosphocreatine.[43] Recent evidence indicates a role for creatine in promoting cancer progression and metastasis.[44–47] In our GBM ST-seq analysis, we observed enrichment of creatine metabolism in various cell populations, with the exception of spots classified as Cluster 3 (Figures 4A and 4B). Notably, in GBM2-R1, the enrichment of creatine metabolism in Cluster 3 spots
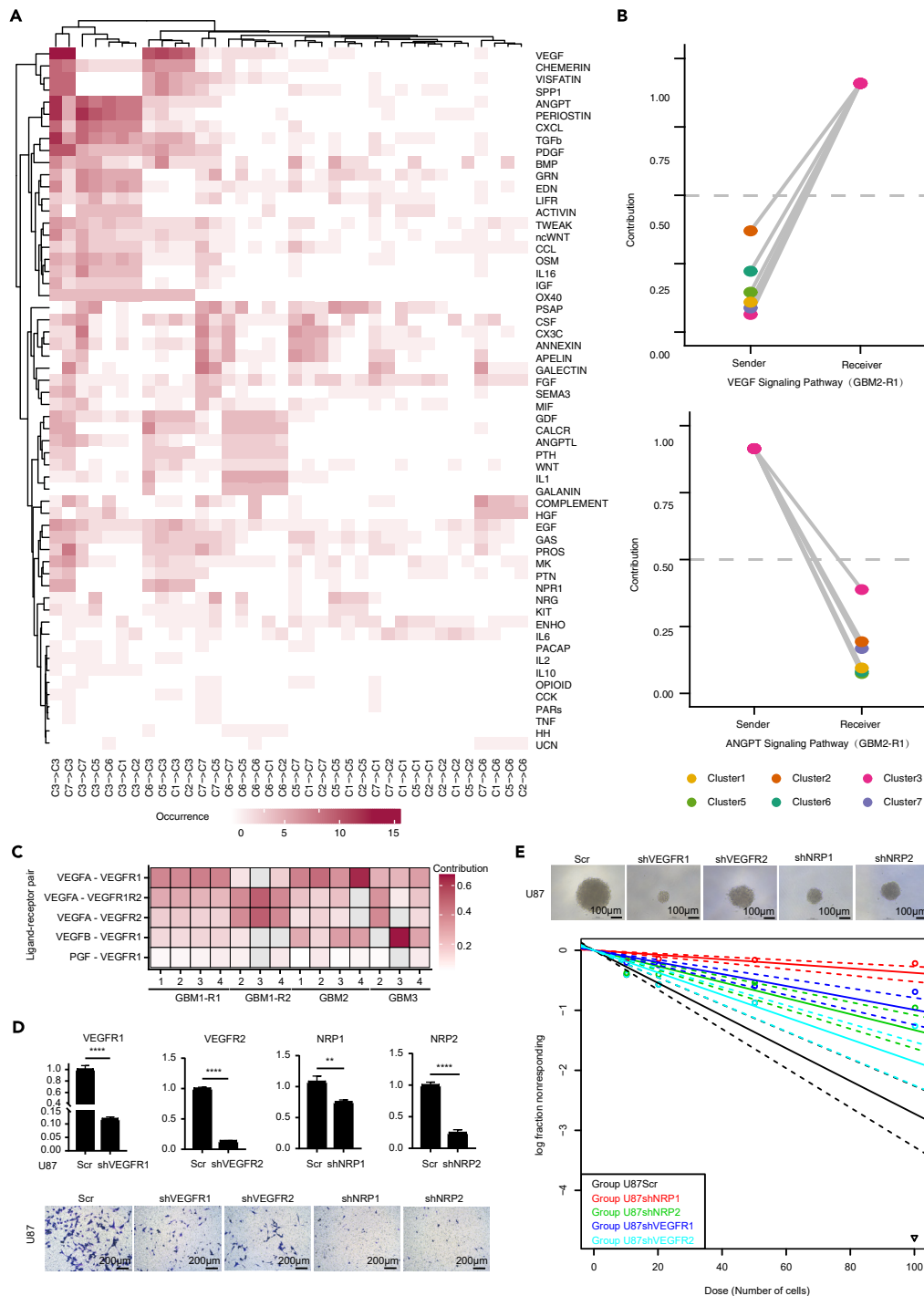
Figure 3. Spatial crosstalk signaling network in GBM

(A) Heatmap representing the comprehensive analysis of ligand-receptor pairs between clusters across all sequenced samples. In total, 58 distinct ligand-receptor pairs were identified.

(B) Focused cluster-based examination of ligand-receptor interactions involving VEGF and ANGPT within the context of GBM2-R1.

(C) Systematic analysis of ligand-receptor pairs pertaining to VEGF across all sequenced samples.

(D) Utilizing Transwell assays, GBM cell line U87 was subjected to shRNA-based targeting of VEGF receptor 1 and 2 (VEGFR1/2) and scramble-RNA to disrupted the ligand-receptor interaction, respectively. Top: migrated cell was quantified and compared. Bars represent mean ± SD, n = 3. p value was

Figure 3. *Continued*

calculated using two-sided unpaired t test. **p < 0.01; ****p < 0.0001, n = 3. Bottom, representative images of three independent experiments are provided. Scale bars, 200 μm.

(E) Extreme limiting dilution analysis was performed using GBM cell line U87 treated with shRNA targeting VEGF receptor 1 and 2 (VEGFR1/2) and scramble-RNA to disrupt the ligand-receptor interaction, respectively. Probability estimates and frequency calculations were computed using the ELDA software.[59] Scale bars, 100 μm.

(enriched with the MES subtype) was markedly lower compared to adjacent Cluster 5 spots with the CL subtype (Figures 4A and 4B). Furthermore, the enrichment of creatine metabolism in the cell population defined as Cluster 7, situated at the peritumoral region, may be associated with its potential to promote tumor infiltration and metastasis.

As elucidated earlier, we identified metabolic distinctions among GBM subtypes, prompting a correlation analysis to unveil key metabolic pathways specific to a subtype. Here, we focused on MES subtype, known for its heightened malignancy in GBM. The correlation analysis, centered on altered metabolic pathways in GBM patients with the MES subtype and utilizing 16 sequenced samples from three patients, unveiled a positive association between the MES subtype and several pivotal metabolic pathways. Specifically, the lysophospholipid pathway, amino sugar and nucleotide sugar metabolism, nicotinate and nicotinamide metabolism, folate metabolism, galactose metabolism, taurine and hypotaurine metabolism, and porphyrins metabolism were markedly and positively correlated with the MES subtype (Figure 4C). Zooming in on the metabolic signaling pathways that exhibited a substantial positive correlation with the MES subtypes, the correlation analysis of the selected seven metabolic signaling pathways present in the peritumor region demonstrated non-significant correlations with CL subtype spots situated in the rapidly proliferating tumor areas. Conversely, these pathways showed a negative correlation with PN subtype spots, which were sparsely distributed within the tumors (Figure S8A). These findings underscore the intrinsic disparities among the PN, CL, and MES subtypes when viewed through the lens of metabolism.

Although the previously mentioned pathways exhibited positive correlations with the MES subtype, they displayed diverse patterns across samples (Figure S8B). Notably, Folate metabolism, a pathway associated with vitamins, was prominently enriched in Cluster 7 among the 16 sequenced samples. In contrast, nicotinate and nicotinamide metabolism showed significant enrichment in Cluster 3 within GBM1-R1-1 to GBM1-R1-4 but exhibited no enrichment in any cluster of GBM2-R1. Furthermore, amino sugar and nucleotide sugar metabolism, as well as porphyrins metabolism, were not enriched in any spot clusters of GBM2-R4. These findings underscore the presence of both inter- and intra-tumor metabolic heterogeneity.

Subsequently, we managed to establish the correlation between metabolic with pathological heterogeneity. Blood vessels within tumors supply nutrients and oxygen but often fail to meet the increasing demands of a growing tumor. The proximity to blood vessels influences tumor characteristics, with cancer cells near vessels showing intense metabolism, defying the Warburg principle through oxidative phosphorylation.[48] Here, we focused on the vessel-enriched Cluster 3. We stratified spots perpendicular to Cluster 3 into layers of five consecutive spots to explore metabolic changes relative to vessel proximity. As shown in Figure S9A, three layers were delineated by Cluster 3: "inner" (I) and "outer" (O). Unsupervised clustering analysis revealed significant distinctions among spots within distinct layers (Figures S9B and S9C). We then examined changes in hypoxia signaling pathways vertically relative to vessel proximity. And we found that Cluster 3 has the lowest hypoxia signaling enrichment, increasing toward the peritumoral brain parenchyma and tumor center (Figure S9D). Similarly, glycolysis, gluconeogenesis, and oxidative phosphorylation show trends mirroring hypoxia signaling, being lowest in Cluster 3 and increasing toward the tumor core and peritumoral regions (Figures S9E–S9G). These findings suggest significant alterations in oxygen supply and metabolism occur at the microscopic level with changing distances from blood vessels.

mTOR signaling, a metabolic regulator responding to cellular energy and key metabolite availability, plays a crucial role in tumorigenesis and cancer cell characteristics.[49,50] Functional evidence also support the mTOR dependence in tumor aggressiveness and resistance.[48] Accordingly, we assessed mTOR pathway enrichment relative to vessel distance perpendicular to Cluster 3. Figure S9H indicates enrichment in all clusters except C3I1 and C3I2, with the outer direction of Cluster 3 exhibiting the most significant enrichment. This region, bordering peritumoral infiltration, shows heightened mTOR activity, suggesting enhanced migratory or invasive capabilities (Figure S9I). Cluster 3, rich in tissue stem cells and GBM MES subtypes, further underscores the association between mTOR enrichment and invasive behavior in this region.

DISCUSSION

Tumor heterogeneity poses a significant challenge in the treatment of GBM. In this study, we conducted genome-wide transcriptome measurements on three GBM samples characterized by high heterogeneity, achieving a spatial resolution of 55 μm. Through sequential comparisons from the peritumoral region to the center of necrosis, we observed that, irrespective of the location within the tumor area—whether near the tumor periphery or at the necrotic site—MES subtypes with higher malignancy were notably enriched in the perivascular area of the tumor. This observation suggests a potential association with vascular metastasis to adjacent normal brain regions. The necrotic area within the tumor arises from the tumor's rapid proliferation, leading to the depletion of nutrients or oxygen supply within the tumor mass. The positive correlation between MES subtypes and tissue stem cells present in Cluster 3, aggregated around blood vessels, may contribute to enhanced tumor cell proliferation and infiltration into the adjacent peritumoral area.

MSCs are ubiquitously found in various tissues, including brain tissue, where they are predominantly located in close proximity to blood vessels.[51] Glioma-associated MSCs have been implicated in facilitating tumor invasion by promoting new angiogenesis and preserving the stemness of tumor stem cells.[52] Consistent with prior research, our analysis of ST data unveiled that MSC cell subtypes were exclusively
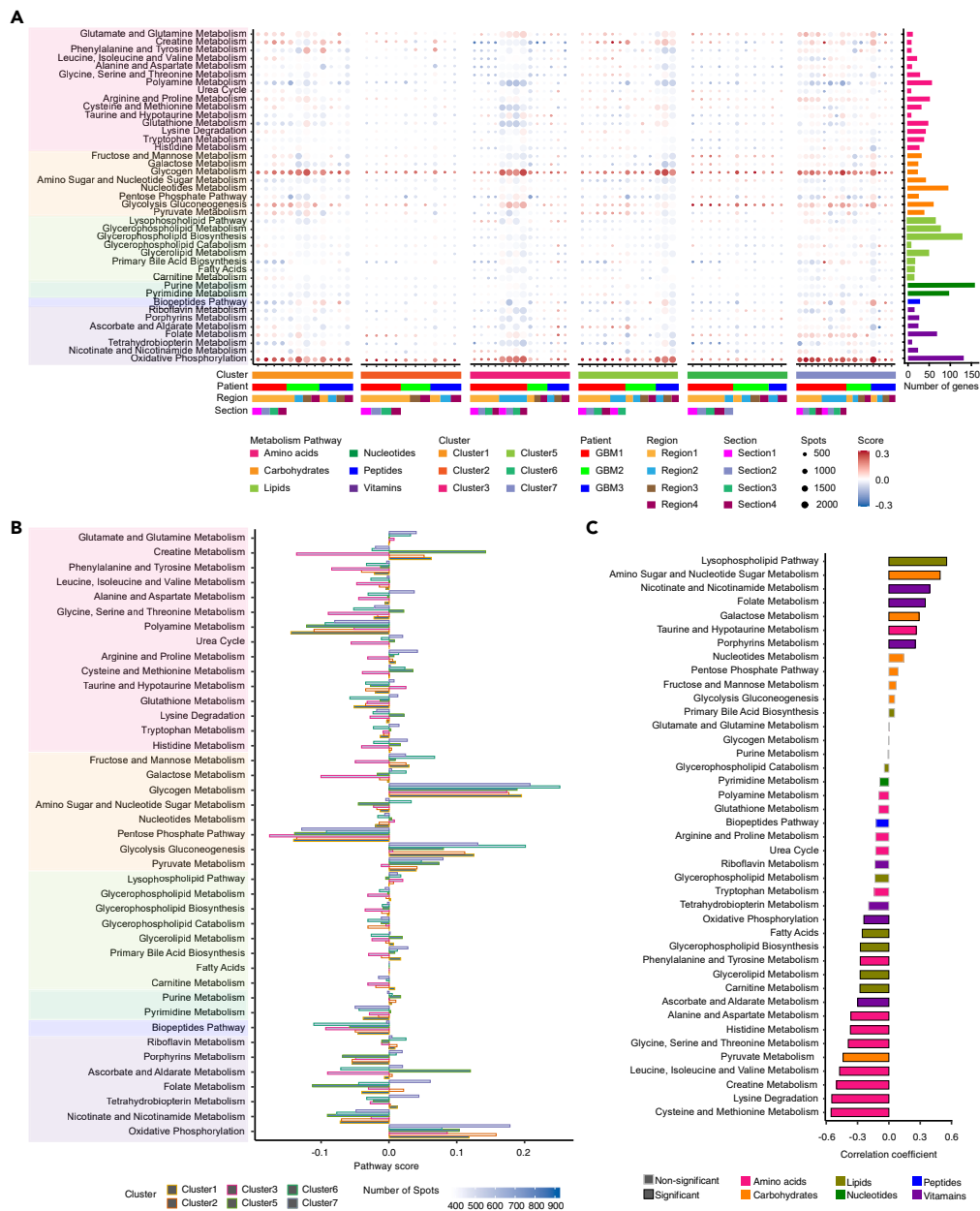
Figure 4. Deciphering metabolic landscapes in GBM

(A) Bubble plot depicting the comprehensive landscape of altered metabolic programs observed in GBM patients. Each bubble represents a specific metabolic program, and its size corresponds to the magnitude of alteration.

(B) Barplot providing a detailed view of the altered metabolic programs within the specific context of GBM2-R1.

(C) Correlation analysis conducted to establish the relationships between the altered metabolic pathway observed in GBM patients and the MES subtype within the GBM2-R1 sample.

identified in spots belonging to Cluster 3, positioned adjacent to blood vessels. Fibroblasts, which may originate from MSC cells, exhibit significant similarities to mesenchymal stem cells when activated. They play a pivotal role in promoting tumor initiation, proliferation, invasion, epithelial-mesenchymal transition, metastasis, and alterations in tumor metabolism.[53] Intriguingly, our cell-type analysis disclosed that fibroblasts were exclusively present in spots belonging to Cluster 3, aligning with the distribution of MES cells. With the enrichment of stem cell signatures and MES subtypes in the cell population defined as Cluster 3, the presence of MSCs and fibroblast cell types may contribute to the promotion of tumor malignancy. Therefore, a more in-depth analysis of cell types, particularly focusing on the fibroblast population, holds the potential to provide a clearer understanding of the contribution of the GBM stroma to tumor progression.

We conducted a comprehensive analysis of cell-cell communication between distinct spot clusters. Spots situated in the perivascular area, grouped into Cluster 3 and enriched with tissue stem signatures and MES subtypes, exhibited a significant enrichment of VEGF signals and functioned as the primary recipients of VEGF signals. Notably, these spots also emitted robust ANGPT signals that exerted an influence on adjacent spots. Both VEGF and ANGPT signals are well established as critical factors in promoting tumor angiogenesis and malignant progression.[35,37,38,54] Considering that VEGF-mediated signaling occurs in tumor cells and contributes to pivotal aspects of tumorigenesis, such as the function of CSCs and tumor initiation, the observed reduction in cell migration and self-renewal abilities after VEGFR knockdown underscores the angiogenesis-independent tumor-promoting role of the VEGF signaling pathway. Furthermore, the enrichment of VEGF, CXCL, transforming growth factor β (TGF-β), CCL, and interleukin-16 (IL-16) signals in spots classified as Cluster 3, which were found to be fibroblast-distributed across all analyzed samples, suggests that fibroblasts enriched in this region may play a tumor-promoting role consistent with cancer-associated fibroblasts.

Metabolic reprogramming stands out as a hallmark of cancer and holds promise as a therapeutic target.[55–57] Our transcriptome-based metabolic enrichment analysis unveils that the metabolic pathway enriched by GBM cells, characterized as the MES subtype, is mutually exclusive with the GBM cell subpopulation defined as PN, aligning with findings from Prabhu AH's article.[40] Despite the diverse molecular pathways propelling gliomagenesis, metabolic programs designed to sustain the aggressive phenotype of this malignancy appear to be conserved within its intricate tumor ecosystem.[39,40,55,58] In the ST-seq dataset under investigation, we observed the metabolic pathways commonly altered across both inter- and intra-tumoral compartments, including glycogen metabolism, glycolysis and gluconeogenesis, and OXPHOS. These metabolic changes were uniformly enriched in all cell types, irrespective of their pathological classification. In contrast, creatine metabolism was selectively enriched in specific spot populations, notably excluding spot classified as Cluster 3, primarily found in vascular-rich regions. These observed alterations in tumor metabolism suggest that tumors adeptly adapt to their microenvironment by orchestrating nutrient shuttling, thereby ensuring sufficient nutritional support for tumor growth and progression.

Our data analyses provide valuable insights into cell-type composition, cell-cell communication, and cell metabolism. However, a limitation of our study is the relatively small sample size, as we collected samples from only three GBM patients who had not undergone chemotherapy or radiotherapy before surgery. A more extensive dataset, encompassing samples from a larger cohort of GBM patients, both with and without prior chemotherapy or radiotherapy, is crucial for a thorough investigation and enhanced clinical applicability. Additionally, our experimental approach has limitations in that the captured and sequenced cells in each spot encompass multiple cells, ranging from approximately 2 to 40 cells per spot. This introduces bias in defining the cell type or GBM subtype for each spot, hindering our ability to finely map cell-cell communications. A parallel single-cell RNA-seq analysis conducted alongside the ST datasets on the corresponding samples would contribute to a more accurate definition of cell types. Addressing these limitations would further enhance the robustness and applicability of our findings.

In summary, we harnessed the power of ST-seq technology to construct a comprehensive genome-wide spatial transcriptome map of GBM. Our findings revealed profound global and local intratumor heterogeneity within tumors and TME, as elucidated through cell subtypes, cell communication, and metabolic analyses. Notably, tumor clusters originating from different patients or distinct tumor locations within the same patient showcased distinctive spatial patterns and transcriptomic diversities. These results provide invaluable insights into the intricate biology of GBM, shedding light on the complex interplay of cellular elements and signaling pathways within the tumor landscape. Such insights hold significant implications for the development of innovative therapeutic strategies geared toward addressing the diverse molecular and spatial characteristics of GBM, ultimately propelling the field toward more effective treatment approaches.

Limitations of the study

This study aims to unveil spatial intricacies of inter- and intra-GBM heterogeneity. We collected samples from only three GBM patients who had not received chemotherapy or radiotherapy prior to surgery. A more extensive dataset, incorporating samples from a larger cohort of GBM patients, both with and without prior chemotherapy or radiotherapy, is crucial for a thorough investigation. Furthermore, our experimental methodology presents limitations, as the cells captured and sequenced in each spot comprise a range of 2–40 cells per spot. This introduces bias in defining cell types or GBM subtypes for each spot, impeding our ability to finely map cell-cell communications. A concurrent single-cell RNA-seq analysis conducted alongside the ST datasets on the corresponding samples would enhancer the precision of definition of cell-type definitions.

STAR★METHODS

Detailed methods are provided in the online version of this paper and include the following:

- KEY RESOURCES TABLE
- RESOURCE AVAILABILITY
  - Lead contact
  - Materials availability
  - Data and code availability
- EXPERIMENTAL MODEL AND STUDY PARTICIPANT DETAILS
- METHOD DETAILS
  - Outline of the spatial transcriptomics workflow

- ○ Staining and imaging
- ○ Permeabilization and reverse transcription
- ○ Second strand synthesis & denaturation
- ○ cDNA library preparation for sequencing
- ○ Sequence alignment and generation of gene expression database
- ○ Spatial gene expression analysis and visualization
- ○ Cell culture
- ○ Transwell assay
- ○ Extreme limiting dilution analysis
- ● QUANTIFICATION AND STATISTICAL ANALYSIS

SUPPLEMENTAL INFORMATION

Supplemental information can be found online at https://doi.org/10.1016/j.isci.2024.110064.

AUTHOR CONTRIBUTIONS

X.W., X.L., B.W., X.Y., and M.J.L. designed the initial study. X.Y. and X.L. analyzed and interpreted the data and drafted the article and figures. B.W. provided samples and contributed histopathological expertise. All authors reviewed and commented on the manuscript.

DECLARATION OF INTERESTS

The authors declare no competing interests.

REFERENCES

1. Bhat, K.P.L., Balasubramaniyan, V., Vaillant, B., Ezhilarasan, R., Hummelink, K., Hollingsworth, F., Wani, K., Heathcock, L., James, J.D., Goodman, L.D., et al. (2013). Mesenchymal differentiation mediated by NF-κB promotes radiation resistance in glioblastoma. Cancer Cell 24, 331–346. https://doi.org/10.1016/j.ccr.2013.08.001.

2. Chen, J., Li, Y., Yu, T.S., McKay, R.M., Burns, D.K., Kernie, S.G., and Parada, L.F. (2012). A restricted cell population propagates glioblastoma growth after chemotherapy. Nature 488, 522–526. https://doi.org/10.1038/nature11287.

3. Shergalis, A., Bankhead, A., 3rd, Luesakul, U., Muangsin, N., and Neamati, N. (2018). Current Challenges and Opportunities in Treating Glioblastoma. Pharmacol. Rev. 70, 412–445. https://doi.org/10.1124/pr.117.014944.

4. Patel, A.P., Tirosh, I., Trombetta, J.J., Shalek, A.K., Gillespie, S.M., Wakimoto, H., Cahill, D.P., Nahed, B.V., Curry, W.T., Martuza, R.L., et al. (2014). Single-cell RNA-seq highlights intratumoral heterogeneity in primary glioblastoma. Science 344, 1396–1401. https://doi.org/10.1126/science.1254257.

5. Neftel, C., Laffy, J., Filbin, M.G., Hara, T., Shore, M.E., Rahme, G.J., Richman, A.R., Silverbush, D., Shaw, M.L., Hebert, C.M., et al. (2019). An Integrative Model of Cellular States, Plasticity, and Genetics for Glioblastoma. Cell 178, 835–849.e21. https://doi.org/10.1016/j.cell.2019.06.024.

6. Wang, L.B., Karpova, A., Gritsenko, M.A., Kyle, J.E., Cao, S., Li, Y., Rykunov, D., Colaprico, A., Rothstein, J.H., Hong, R., et al. (2021). Proteogenomic and metabolomic characterization of human glioblastoma. Cancer Cell 39, 509–528.e20. https://doi.org/10.1016/j.cell.2021.01.006.

7. Cang, Z., and Nie, Q. (2020). Inferring spatial and signaling relationships between cells from single cell transcriptomic data. Nat. Commun. 11, 2084. https://doi.org/10.1038/s41467-020-15968-5.

8. Svensson, V., Vento-Tormo, R., and Teichmann, S.A. (2018). Exponential scaling of single-cell RNA-seq in the past decade. Nat. Protoc. 13, 599–604. https://doi.org/10.1038/nprot.2017.149.

9. Zhang, L., He, X., Liu, X., Zhang, F., Huang, L.F., Potter, A.S., Xu, L., Zhou, W., Zheng, T., Luo, Z., et al. (2019). Single-Cell Transcriptomics in Medulloblastoma Reveals Tumor-Initiating Progenitors and Oncogenic Cascades during Tumorigenesis and Relapse. Cancer Cell 36, 302–318.e7. https://doi.org/10.1016/j.ccell.2019.07.009.

10. Yu, K., Hu, Y., Wu, F., Guo, Q., Qian, Z., Hu, W., Chen, J., Wang, K., Fan, X., Wu, X., et al. (2020). Surveying brain tumor heterogeneity by single-cell RNA-sequencing of multi-sector biopsies. Natl. Sci. Rev. 7, 1306–1318. https://doi.org/10.1093/nsr/nwaa099.

11. Zhang, M., Yang, H., Wan, L., Wang, Z., Wang, H., Ge, C., Liu, Y., Hao, Y., Zhang, D., Shi, G., et al. (2020). Single-cell transcriptomic architecture and intercellular crosstalk of human intrahepatic cholangiocarcinoma. J. Hepatol. 73, 1118–1130. https://doi.org/10.1016/j.jhep.2020.05.039.

12. Castellan, M., Guarnieri, A., Fujimura, A., Zanconato, F., Battilana, G., Panciera, T., Sladitschek, H.L., Contessotto, P., Citron, A., Grilli, A., et al. (2021). Single-cell analyses reveal YAP/TAZ as regulators of stemness and cell plasticity in Glioblastoma. Nat. Cancer 2, 174–188. https://doi.org/10.1038/s43018-020-00150-z.

13. Salmen, F., Stahl, P.L., Mollbrink, A., Navarro, J.F., Vickovic, S., Frisen, J., and Lundeberg, J. (2018). Barcoded solid-phase RNA capture for Spatial Transcriptomics profiling in mammalian tissue sections. Nat. Protoc. 13,

2501–2534. https://doi.org/10.1038/s41596-018-0045-2.

14. Ståhl, P.L., Salmén, F., Vickovic, S., Lundmark, A., Navarro, J.F., Magnusson, J., Giacomello, S., Asp, M., Westholm, J.O., Huss, M., et al. (2016). Visualization and analysis of gene expression in tissue sections by spatial transcriptomics. Science 353, 78–82. https://doi.org/10.1126/science.aaf2403.

15. Fawkner-Corbett, D., Antanaviciute, A., Parikh, K., Jagielowicz, M., Gerós, A.S., Gupta, T., Ashley, N., Khamis, D., Fowler, D., Morrissey, E., et al. (2021). Spatiotemporal analysis of human intestinal development at single-cell resolution. Cell 184, 810–826.e23. https://doi.org/10.1016/j.cell.2020.12.016.

16. Asp, M., Giacomello, S., Larsson, L., Wu, C., Fürth, D., Qian, X., Wärdell, E., Custodio, J., Reimegård, J., Salmén, F., et al. (2019). A Spatiotemporal Organ-Wide Gene Expression and Cell Atlas of the Developing Human Heart. Cell 179, 1647–1660.e19. https://doi.org/10.1016/j.cell.2019.11.025.

17. Berglund, E., Maaskola, J., Schultz, N., Friedrich, S., Marklund, M., Bergenstråhle, J., Tarish, F., Tanoglidi, A., Vickovic, S., Larsson, L., et al. (2018). Spatial maps of prostate cancer transcriptomes reveal an unexplored landscape of heterogeneity. Nat. Commun. 9, 2419. https://doi.org/10.1038/s41467-018-04724-5.

18. Ravi, V.M., Neidert, N., Will, P., Joseph, K., Maier, J.P., Kückelhaus, J., Vollmer, L., Goeldner, J.M., Behringer, S.P., Scherer, F., et al. (2020). Lineage and Spatial Mapping of Glioblastoma-Associated Immunity. Preprint at bioRxiv. https://doi.org/10.1101/2020.06.01.121467.

19. Wu, R., Guo, W., Qiu, X., Wang, S., Sui, C., Lian, Q., Wu, J., Shan, Y., Yang, Z., Yang, S., et al. (2021). Comprehensive analysis of spatial architecture in primary liver cancer. Sci. Adv. 7, eabg3750. https://doi.org/10.1126/sciadv.abg3750.

20. Liu, Y., Yang, M., Deng, Y., Su, G., Enninful, A., Guo, C.C., Tebaldi, T., Zhang, D., Kim, D., Bai, Z., et al. (2020). High-Spatial-Resolution Multi-Omics Sequencing via Deterministic Barcoding in Tissue. Cell 183, 1665–1681.e18. https://doi.org/10.1016/j.cell.2020.10.026.

21. Stickels, R.R., Murray, E., Kumar, P., Li, J., Marshall, J.L., Di Bella, D.J., Arlotta, P., Macosko, E.Z., and Chen, F. (2021). Highly sensitive spatial transcriptomics at near-cellular resolution with Slide-seqV2. Nat. Biotechnol. 39, 313–319. https://doi.org/10.1038/s41587-020-0739-1.

22. Rodriques, S.G., Stickels, R.R., Goeva, A., Martin, C.A., Murray, E., Vanderburg, C.R., Welch, J., Chen, L.M., Chen, F., and Macosko, E.Z. (2019). Slide-seq: A scalable technology for measuring genome-wide expression at high spatial resolution. Science 363, 1463–1467. https://doi.org/10.1126/science.aaw1219.

23. Janesick, A., Shelansky, R., Gottscho, A.D., Wagner, F., Williams, S.R., Rouault, M., Beliakoff, G., Morrison, C.A., Oliveira, M.F., Sicherman, J.T., et al. (2023). High resolution mapping of the tumor microenvironment using integrated single-cell, spatial and in situ analysis. Nat. Commun. 14, 8353. https://doi.org/10.1038/s41467-023-43458-x.

24. Stuart, T., Butler, A., Hoffman, P., Hafemeister, C., Papalexi, E., Mauck, W.M., Hao, Y., Stoeckius, M., Smibert, P., and Satija, R. (2019). Comprehensive Integration of Single-Cell Data. Cell 177, 1888–1902.e21. https://doi.org/10.1016/j.cell.2019.05.031.

25. Zhao, E., Stone, M.R., Ren, X., Guenthoer, J., Smythe, K.S., Pulliam, T., Williams, S.R., Uytingco, C.R., Taylor, S.E.B., Nghiem, P., et al. (2021). Spatial transcriptomics at subspot resolution with BayesSpace. Nat. Biotechnol. 39, 1375–1384. https://doi.org/10.1038/s41587-021-00935-2.

26. Xie, X.P., Laks, D.R., Sun, D., Ganbold, M., Wang, Z., Pedraza, A.M., Bale, T., Tabar, V., Brennan, C., Zhou, X., and Parada, L.F. (2022). Quiescent human glioblastoma cancer stem cells drive tumor initiation, expansion, and recurrence following chemotherapy. Dev. Cell 57, 32–46.e8. https://doi.org/10.1016/j.devcel.2021.12.007.

27. Greenwald, A.C., Darnell, N.G., Hoefflin, R., Simkin, D., Mount, C.W., Gonzalez Castro, L.N., Harnik, Y., Dumont, S., Hirsch, D., Nomura, M., et al. (2024). Integrative spatial analysis reveals a multi-layered organization of glioblastoma. Cell 187, 2485–2501.e26. https://doi.org/10.1016/j.cell.2024.03.029.

28. Chanoch-Myers, R., Wider, A., Suva, M.L., and Tirosh, I. (2022). Elucidating the diversity of malignant mesenchymal states in glioblastoma by integrative analysis. Genome Med. 14, 106. https://doi.org/10.1186/s13073-022-01109-8.

29. El Andaloussi, S., Mäger, I., Breakefield, X.O., and Wood, M.J.A. (2013). Extracellular vesicles: biology and emerging therapeutic opportunities. Nat. Rev. Drug Discov. 12, 347–357. https://doi.org/10.1038/nrd3978.

30. Hinshaw, D.C., and Shevde, L.A. (2019). The Tumor Microenvironment Innately Modulates Cancer Progression. Cancer Res. 79, 4557–4566. https://doi.org/10.1158/0008-5472.CAN-18-3962.

31. Karakasheva, T.A., Lin, E.W., Tang, Q., Qiao, E., Waldron, T.J., Soni, M., Klein-Szanto, A.J., Sahu, V., Basu, D., Ohashi, S., et al. (2018). IL-6 Mediates Cross-Talk between Tumor Cells and Activated Fibroblasts in the Tumor Microenvironment. Cancer Res. 78, 4957–4970. https://doi.org/10.1158/0008-5472.CAN-17-2268.

32. Klemm, F., Maas, R.R., Bowman, R.L., Kornete, M., Soukup, K., Nassiri, S., Brouland, J.P., Iacobuzio-Donahue, C.A., Brennan, C., Tabar, V., et al. (2020). Interrogation of the Microenvironmental Landscape in Brain Tumors Reveals Disease-Specific Alterations of Immune Cells. Cell 181, 1643–1660.e17. https://doi.org/10.1016/j.cell.2020.05.007.

33. Broekman, M.L., Maas, S.L.N., Abels, E.R., Mempel, T.R., Krichevsky, A.M., and Breakefield, X.O. (2018). Multidimensional communication in the microenvirons of glioblastoma. Nat. Rev. Neurol. 14, 482–495. https://doi.org/10.1038/s41582-018-0025-8.

34. Jin, S., Guerrero-Juarez, C.F., Zhang, L., Chang, I., Ramos, R., Kuan, C.-H., Myung, P., Plikus, M.V., and Nie, Q. (2021). Inference and analysis of cell-cell communication using CellChat. Nat. Commun. 12, 1088. https://doi.org/10.1038/s41467-021-21246-9.

35. Goel, H.L., and Mercurio, A.M. (2013). VEGF targets the tumour cell. Nat. Rev. Cancer 13, 871–882. https://doi.org/10.1038/nrc3627.

36. Elaimy, A.L., and Mercurio, A.M. (2018). Convergence of VEGF and YAP/TAZ signaling: Implications for angiogenesis and cancer biology. Sci. Signal. 11, eaau1165. https://doi.org/10.1126/scisignal.aau1165.

37. Molnar, N., and Siemann, D.W. (2013). Combined Ang-2 and VEGF Targeting Therapies in Renal Cell Carcinoma. J. Cancer Ther. 04, 1–6. https://doi.org/10.4236/jct.2013.49A2001.

38. Biel, N.M., and Siemann, D.W. (2016). Targeting the Angiopoietin-2/Tie-2 axis in conjunction with VEGF signal interference. Cancer Lett. 380, 525–533. https://doi.org/10.1016/j.canlet.2014.09.035.

39. Libby, C.J., Tran, A.N., Scott, S.E., Griguer, C., and Hjelmeland, A.B. (2018). The pro-tumorigenic effects of metabolic alterations in glioblastoma including brain tumor initiating cells. Biochim. Biophys. Acta Rev. Canc 1869, 175–188. https://doi.org/10.1016/j.bbcan.2018.01.004.

40. Prabhu, A.H., Kant, S., Kesarwani, P., Ahmed, K., Forsyth, P., Nakano, I., and Chinnaiyan, P. (2019). Integrative cross-platform analyses identify enhanced heterotrophy as a metabolic hallmark in glioblastoma. Neuro Oncol. 21, 337–347. https://doi.org/10.1093/neuonc/noy185.

41. Vander Heiden, M.G., Cantley, L.C., and Thompson, C.B. (2009). Understanding the Warburg effect: the metabolic requirements of cell proliferation. Science 324, 1029–1033. https://doi.org/10.1126/science.1160809.

42. Wolf, A., Agnihotri, S., Micallef, J., Mukherjee, J., Sabha, N., Cairns, R., Hawkins, C., and Guha, A. (2011). Hexokinase 2 is a key mediator of aerobic glycolysis and promotes tumor growth in human glioblastoma multiforme. J. Exp. Med. 208, 313–326. https://doi.org/10.1084/jem.20101470.

43. Zhang, L., and Bu, P. (2022). The two sides of creatine in cancer. Trends Cell Biol. 32, 380–390. https://doi.org/10.1016/j.tcb.2021.11.004.

44. Loo, J.M., Scherl, A., Nguyen, A., Man, F.Y., Weinberg, E., Zeng, Z., Saltz, L., Paty, P.B., and Tavazoie, S.F. (2015). Extracellular Metabolic Energetics Can Promote Cancer Progression. Cell 160, 393–406. https://doi.org/10.1016/j.cell.2014.12.018.

45. Zhang, L., Zhu, Z., Yan, H., Wang, W., Wu, Z., Zhang, F., Zhang, Q., Shi, G., Du, J., Cai, H., et al. (2021). Creatine promotes cancer metastasis through activation of Smad2/3. Cell Metab. 33, 1111–1123.e4. https://doi.org/10.1016/j.cmet.2021.03.009.

46. Maguire, O.A., Ackerman, S.E., Szwed, S.K., Maganti, A.V., Marchildon, F., Huang, X., Kramer, D.J., Rosas-Villegas, A., Gelfer, R.G., Turner, L.E., et al. (2021). Creatine-mediated crosstalk between adipocytes and cancer cells regulates obesity-driven breast cancer. Cell Metab. 33, 499–512.e6. https://doi.org/10.1016/j.cmet.2021.01.018.

47. Papalazarou, V., Zhang, T., Paul, N.R., Juin, A., Cantini, M., Maddocks, O.D.K., Salmeron-Sanchez, M., and Machesky, L.M. (2020). The creatine–phosphagen system is mechanoresponsive in pancreatic adenocarcinoma and fuels invasion and metastasis. Nat. Metab. 2, 62–80. https://doi.org/10.1038/s42255-019-0159-z.

48. Kumar, S., Sharife, H., Kreisel, T., Mogilevsky, M., Bar-Lev, L., Grunewald, M., Aizenshtein, E., Karni, R., Paldor, I., Shlomi, T., and Keshet, E. (2019). Intra-Tumoral Metabolic Zonation and Resultant Phenotypic Diversification Are Dictated by Blood Vessel Proximity. Cell Metab. 30, 201–211.e6. https://doi.org/10.1016/j.cmet.2019.04.003.

49. Liu, G.Y., and Sabatini, D.M. (2020). mTOR at the nexus of nutrition, growth, ageing and disease. Nat. Rev. Mol. Cell Biol. 21, 183–203. https://doi.org/10.1038/s41580-019-0199-y.

50. Saxton, R.A., and Sabatini, D.M. (2017). mTOR Signaling in Growth, Metabolism, and Disease. Cell 168, 960–976. https://doi.org/10.1016/j.cell.2017.02.004.

51. Kang, S.-G., Shinojima, N., Hossain, A., Gumin, J., Yong, R.L., Colman, H., Marini, F., Andreeff, M., and Lang, F.F. (2010). Isolation and Perivascular Localization of Mesenchymal Stem Cells From Mouse Brain. Neurosurgery *67*, 711–720. https://doi.org/10.1227/01.Neu.0000377859.06219.78.

52. Kong, B.H., Shin, H.-D., Kim, S.-H., Mok, H.-S., Shim, J.-K., Lee, J.-H., Shin, H.-J., Huh, Y.-M., Kim, E.-H., Park, E.-K., et al. (2013). Increased in vivo angiogenic effect of glioma stromal mesenchymal stem-like cells on glioma cancer stem cells from patients with glioblastoma. Int. J. Oncol. *42*, 1754–1762. https://doi.org/10.3892/ijo.2013.1856.

53. Kalluri, R. (2016). The biology and function of fibroblasts in cancer. Nat. Rev. Cancer *16*, 582–598. https://doi.org/10.1038/nrc.2016.73.

54. O'Connell, J.T., Sugimoto, H., Cooke, V.G., MacDonald, B.A., Mehta, A.I., LeBleu, V.S., Dewar, R., Rocha, R.M., Brentani, R.R., Resnick, M.B., et al. (2011). VEGF-A and Tenascin-C produced by S100A4+ stromal cells are important for metastatic colonization. Proc. Natl. Acad. Sci. USA *108*, 16002–16007. https://doi.org/10.1073/pnas.1109493108.

55. Hoang-Minh, L.B., Siebzehnrubl, F.A., Yang, C., Suzuki-Hatano, S., Dajac, K., Loche, T., Andrews, N., Schmoll Massari, M., Patel, J., Amin, K., et al. (2018). Infiltrative and drug-resistant slow-cycling cells support metabolic heterogeneity in glioblastoma. EMBO J. *37*, e98772. https://doi.org/10.15252/embj.201798772.

56. Rusu, P., Shao, C., Neuerburg, A., Acikgöz, A.A., Wu, Y., Zou, P., Phapale, P., Shankar, T.S., Döring, K., Dettling, S., et al. (2019). GPD1 Specifically Marks Dormant Glioma Stem Cells with a Distinct Metabolic Profile. Cell Stem Cell *25*, 241–257.e8. https://doi.org/10.1016/j.stem.2019.06.004.

57. McGuirk, S., Audet-Delage, Y., and St-Pierre, J. (2020). Metabolic Fitness and Plasticity in Cancer Progression. Trends Cancer *6*, 49–61. https://doi.org/10.1016/j.trecan.2019.11.009.

58. Agnihotri, S., and Zadeh, G. (2016). Metabolic reprogramming in glioblastoma: the influence of cancer metabolism on epigenetics and unanswered questions. Neuro Oncol. *18*, 160–172. https://doi.org/10.1093/neuonc/nov125.

59. Hu, Y., and Smyth, G.K. (2009). ELDA: Extreme limiting dilution analysis for comparing depleted and enriched populations in stem cell and other assays. J. Immunol. Methods *347*, 70–78. https://doi.org/10.1016/j.jim.2009.06.008.

60. Li, Q., Lv, X., Han, C., Kong, Y., Dai, Z., Huo, D., Li, T., Li, D., Li, W., Wang, X., et al. (2022). Enhancer reprogramming promotes the activation of cancer-associated fibroblasts and breast cancer metastasis. Theranostics *12*, 7491–7508. https://doi.org/10.7150/thno.75853.

61. Lv, X., Li, Q., Liu, H., Gong, M., Zhao, Y., Hu, J., Wu, F., and Wu, X. (2022). JUN activation modulates chromatin accessibility to drive TNFα-induced mesenchymal transition in glioblastoma. J. Cell Mol. Med. *26*, 4602–4612. https://doi.org/10.1111/jcmm.17490.

62. Dong, F., Li, Q., Yang, C., Huo, D., Wang, X., Ai, C., Kong, Y., Sun, X., Wang, W., Zhou, Y., et al. (2018). PRMT2 links histone H3R8 asymmetric dimethylation to oncogenic activation and tumorigenesis of glioblastoma. Nat. Commun. *9*, 4552. https://doi.org/10.1038/s41467-018-06968-7.

STAR★METHODS

KEY RESOURCES TABLE

REAGENT or RESOURCE	SOURCE	IDENTIFIER
Biological samples		
Tumor tissue of treatment-naive GBM patient	Tianjin Huanhu Hospital	N/A
Chemicals, peptides, and recombinant proteins		
Hematoxylin, Mayer's (Lillie's Modification)	Agilent	S330930-2
Bluing Buffer, Dako	Agilent	CS70230-2
Eosin Y solution, aqueous, 0.5% (w/v) in water	Millipore Sigma	HT110216-500ML
Tris-base solution	Thermo Fisher Scientific	BP152-500
Glycerol	Millipore Sigma	104094
SSC Buffer 20X Concentrate	Millipore Sigma	S6639-1L
Visium Spatial Gene Expression Slide & Reagent Kit	10x Genomics	16 rxns PN-1000184
Potassium Hydroxide	Millipore Sigma	P4494-50ML
Low TE Buffer (10 mM Tris-HCl pH 8.0, 0.1 mM EDTA)	Thermo Fisher Scientific	12090-015
Tris 1M, pH 7.0, RNase-free	Thermo Fisher Scientific	AM9850G
Ethanol, Pure (200 Proof, anhydrous)	Millipore Sigma	E7023-500ML
2-Propanol (Isopropanol), ≥ 99.5%	Millipore Sigma	I9516-25ML
Methanol, for HPLC, ≥ 99.9%	Millipore Sigma	34860
Acetic acid, ≥ 99.9%	Millipore Sigma	A6283
SPRIselect Reagent Kit	Beckman Coulter	B23318
Qiagen Buffer EB	Qiagen	19086
KAPA SYBR FAST qPCR Master Mix (2X)	KAPA Biosystems	KK4600
Hydrochloric Acid Solution, 0.1N	Fisher Chemical	SA54-1
Deposited data		
Spatial transcriptomics RNA-sequencing data	This paper	GEO: GSE253080
Experimental models: Cell lines		
U87	American Type Culture Collection	N/A
Experimental models: Organisms/strains		
GBM patient 1	Tianjin Huanhu Hospital	Male; 74 years old; WHO grade 4; IDH wild type
GBM patient 2	Tianjin Huanhu Hospital	Female; 72 years old; WHO grade 4; IDH wild type
GBM patient 3	Tianjin Huanhu Hospital	Female; 53 years old; WHO grade 4; IDH wild type
Oligonucleotides		
VEGFR1 knockdown: 5′-GAGAGACTTAAAC TGGGCAAA-3′	This paper	N/A
VEGFR2 knockdown: 5′-GTGCTGTTTCTGACTCCTAAT-3′	This paper	N/A
NRP1 knockdown: 5′-TATACTAGAATCACCGCATTT-3′	This paper	N/A
NRP2 knockdown: 5′-CCTCAACTTCAACCCTCACTT-3′	This paper	N/A

REAGENT or RESOURCE	SOURCE	IDENTIFIER
Software and algorithms		
SpaceRanger	10x Genomics	https://support.10xgenomics.com/spatial-gene-expression/software/downloads/latest
Seurat v3.0.0	Stuart et al.[24]	https://github.com/satijalab/seurat/releases/tag/v3.0.0
BayesSpace	Zhao et al.[25]	http://www.bioconductor.org/packages/release/bioc/html/BayesSpace.html
ELDA	Hu et al.[59]	http://bioinf.wehi.edu.au/software/elda/
CellChat	Jin et al.[34]	https://github.com/sqjin/CellChat

RESOURCE AVAILABILITY

Lead contact

Further information and requests for resources and reagents should be directed to and will be fulfilled by the lead contact, Xudong Wu (wuxudong@tmu.edu.cn).

Materials availability

This study did not generate new unique reagents.

Data and code availability

- Spatial transcriptomics RNA-sequencing data that support the findings of this study have been deposited in the GEO (https://www.ncbi.nlm.nih.gov/geo/info/submission.html) under accession code GSE253080 and will be publicly available as of the date of publication.
- This paper does not report original code.
- Any additional information required to reanalyze the data reported in this paper is available from the lead contact upon request.

EXPERIMENTAL MODEL AND STUDY PARTICIPANT DETAILS

Tumor tissues were procured from patients diagnosed with treatment-naive GBM (WHO Grade 4) at the Tianjin Huanhu Hospital (Tianjin, China). All tumor specimens were authenticated as glioblastoma by trained pathologists. For ST sequencing, 16 fresh tissue samples were extracted via surgery from 3 Han Chinese patients with glioblastoma, 1 sample from males and 2 from females were used in this study (Table S1). No information about socioeconomic status was collected for the participants. The GBM tumor specimens were promptly frozen in liquid nitrogen and embedded in OCT compound. The frozen tissue specimens were then cryo-sectioned at a thickness of 10 μm. The sections were mounted on pre-treated glass slides and incubated at 37°C for 1 min (min), followed by fixation in methanol for 30 min at −20°C and washing in phosphate buffered saline (PBS). The current ST protocol was applied to all sections, resulting in both conventional hematoxylin and eosin (H&E) images that were amenable to annotation by pathologists, as well as gene expression profiles for each microarray spot.

The study was approved by the Ethics Committee of Tianjin Huanhu Hospital (Application number, NO.2019-14) and conducted in adherence to the Declaration of Helsinki and Good Clinical Practice. All participants were comprehensively informed about the study through complete and adequate verbal and written communications prior to their involvement. Written informed consent was secured from all participating subjects before their enrollment in the study. A thorough review of the clinical information of these patients was conducted, which included factors such as age, tumor size, overall survival (OS), disease-free survival (DFS), among others.

METHOD DETAILS

Outline of the spatial transcriptomics workflow

The ST experiment is based on the Visium Technology Platform of 10X Genomics Visium Platform. The specific product numbers of reagents and consumables in the experiment can be found at https://www.10xgenomics.com/products/spatial-gene-expression.

The ST method adheres to the following workflow: tissue sectioning, tissue fixation, tissue staining, imaging, pre-permeabilization, permeabilization, cDNA synthesis, tissue removal, probe release, library preparation, sequencing, data processing, data visualization, and analysis.

Typically, RNA integrity numbers (RIN) greater than 8 and good tissue morphology were considered suitable for subsequent library construction and sequencing experiments. In the context of ST technology, each section within the capture area (6.5 mm by 6.5 mm) can contain up to 5000 spots, with each spot having a diameter of 55 μm. We define "high-quality data" as sample data with an average number of genes

per feature exceeding 1000, as well as proper tissue placement on the spatial array (tissue within the area, minimal folded areas and missing pieces, etc.).

Staining and imaging

Sections were fixed for 10 min using pre-cooled methanol at −20°C and stained with Mayer's Hematoxylin (#S3309, Dako) and Bluing buffer (#CS702, Dako), followed by Eosin (#HT110216, Sigma-Aldrich) in a Tris-base solution (0.45 M Tris, 0.5 M Acetic acid, pH 6.0). Following rinsing, the dried sections were mounted with 85% Glycerol (#104094, Merck Millipore) and covered with a coverslip (#BB024060A1, Menzel-Glsäer). Bright field imaging was performed using the Automated Quantitative Pathology Imaging System (Perkin Elmer). Raw images were stitched together using ImageScope software. The images were then visualized and exported in JPEG format.

Permeabilization and reverse transcription

For each well, corresponding to each sub-array with a section, 70 μL of Permeabilization Enzyme was added along the side of the wells to uniformly cover the tissue sections, ensuring the absence of bubbles. The Slide Cassette was gently tapped to guarantee uniform coverage, followed by sealing and placing it on the Thermocycler Adaptor at 37°C for 30 min. Subsequently, the Permeabilization Enzyme was removed by washing with 100 μL of 0.1x SSC. Finally, 70 μL of the reverse transcription mix was added to each well to initiate Reverse Transcription.

Second strand synthesis & denaturation

The RT Master Mix was removed from the wells, and 75 μL of 0.08 M Potassium hydroxide (KOH) was added to each well. Following a 5-min incubation at room temperature (RT), the KOH was removed from the wells, and 100 μL of Qiagen Buffer EB (Cat. No. 19086) was added to each well. Subsequently, the Buffer EB was removed from the wells, and 75 μL of the Second Strand Mix was added to each well to initiate Second Strand Synthesis. After incubation, the reagents were removed from the wells, and 100 μL of Buffer EB was added to each well. Then, the Buffer EB was removed from the wells, and 35 μL of 0.08 M KOH was added to each well. After a 10-min incubation at RT, 5 μL of Tris-HCl (1 M, pH 7.0) was added to 4 tubes in an 8-tube strip (4 tubes will be used for each slide). Finally, 35 μL of the sample was transferred from each well to a corresponding tube containing Tris-HCl in the 8-tube strip.

cDNA library preparation for sequencing

One microliter of the sample was transferred to the qPCR plate, and 9 μL of qPCR Mix was added to each well to initiate a qPCR procedure for determining the cycle numbers of subsequent cDNA amplification steps. Next, 65 μL of cDNA Amplification Mix was added to the remaining 34 μL of samples and incubated in a thermal cycler to amplify the cDNA. Following amplification, 60 μL of SPRIselect reagent (0.6 ×) was added to each sample (100 μL in total). Following a 5-min incubation at RT, the tube strip was placed on the magnet·High. Once the solution had clarified, the supernatant was removed, and the pellet was washed twice with 80% ethanol. Then, 40.5 μL of Buffer EB was added. After a 2-min incubation at RT, the tube strip was placed on the magnet•Low. Once again, once the solution had clarified, 40 μL of the sample was transferred to a new tube strip. One μL of the sample was taken for cDNA quality control and quantification using an Agilent Bioanalyzer High Sensitivity chip. Subsequently, the spatial gene expression library construction and sequencing were performed by Novogene Co., Ltd.

Sequence alignment and generation of gene expression database

In each pair of reads, the first read comprised the spatial barcode and the UMI but lacked gene information. The second read contained the gene information and was initially processed using the Burrow-Wheeler Aligner (BWA) for quality trimming. Furthermore, stretches of homopolymers exceeding 15 bases were excised along with the sequences following the homopolymer, and all reads shorter than 28 bases were discarded. The remaining reads were aligned against the human genome (hg38) for GBM samples using Bowtie2 v2.2.3 with default settings. The number of reads aligning to each gene was counted with htseq-count v0.6.1, utilizing RefSeq gene annotations restricted to validated protein-coding and non-coding transcripts (transcript_ids starting with "NM_" or "NR_") for GBM samples. Mitochondrial genes were excluded from the analysis due to their high abundance and potential for internal priming. Whenever read two in a read pair aligned to a gene, the spatial barcode from the corresponding read one was assigned to a barcode in the reference file, as described previously ("de-multiplexing"). To eliminate reads that were duplicated during the amplification protocol, a clustering algorithm that sorts the UMIs and iterates over them to form clusters based on the minimum hamming distance was employed. Ultimately, all the information was written to a file, generating a database that combines gene expression and spatial information.

Spatial gene expression analysis and visualization

Raw sequencing reads were aligned to the reference genome hg38 using SpaceRanger (version 1.2.0) to generate raw gene expression matrices for each sample. Subsequent analysis was conducted using the Seurat R package (version 3.0).[24] In brief, spot with fewer than 1,000 total features were removed. Additionally, spot with more than 30% of expressed mitochondrial genes were discarded. Hence, after unsupervised clustering, we removed cluster 4 due to low counts of captured features and genes was lower than 1000 in per spot in that cluster. All analyses were conducted in accordance with the instructions provided at https://satijalab.org/seurat.

Cell culture

The GBM cell line U87 was obtained from the American Type Culture Collection (Manassas, Virginia, USA) and cultured in Dulbecco's modified Eagle's medium (DMEM) supplemented with 10% fetal bovine serum (FBS) and 1% Penicillin-Streptomycin (PS). Cells were incubated at 37°C in a humidified incubator with 5% CO_2. Cell authentication was performed by examining their karyotypes and morphologies. All cells were tested for mycoplasma contamination using PCR and were confirmed to be mycoplasma-free.

Transwell assay

Transwell chambers with an 8-μm pore size in 24-well plates (Corning) were utilized for the migration assay as previously described.[60,61] In detail, 5×10^4 U87 cells were seeded in the upper chamber using serum-free medium. The lower chamber was filled with 500 μL of DMEM containing 5% FBS as a chemoattractant. Following a 24-h incubation in the incubator, the cells in the upper chamber were carefully removed using a cotton swab. The migrated and invaded cells were washed twice with PBS, fixed with 4% tissue fixative solution, and stained with 0.1% crystal violet for 10 min, respectively. Subsequently, image capture and quantification were performed.

Extreme limiting dilution analysis

The extreme limiting dilution assay were performed as previously described.[62] In brief, U87 cells were resuspended in sphere formation medium (DMEM/F12 supplemented with 1% B27, 20 ng/mL human EGF, 10 ng/mL human b-FGF, and 5 μg/mL insulin) and plated into 96-well plates pre-coated with 0.5% agarose at the specified cell doses (10, 20, 50, and 100 cell per well, respectively). At least 60 wells were seeded with cells for each cell dose. Two weeks later, the number of wells containing spheres was counted, and utilized to calculate the tumor initiating frequency using the ELDA software (http://bioinf.wehi.edu.au/software/elda/).[59]

QUANTIFICATION AND STATISTICAL ANALYSIS

Data are expressed as mean ± SD. Analyses were performed using R or GraphPad Prism V9. p value was calculated using two-sided Student's t test and are shown in footnotes in Figures 2E, 3D, S5C, and S8A. Significance levels are shown in footnotes in Figure 3D and are denoted as follows: **, $p < 0.01$; ****, $p < 0.0001$. The number of replicate determinations is indicated by ''n'', $n = 3$.